

Properties of Contracting Massive Protostellar Cores

*L. E. Pirogov**, *P. M. Zemlyanukha*, *E. M. Dombek*

Gaponov-Grekhov Institute of Applied Physics, Russian Academy of Sciences, Nizhny Novgorod, Russia

* e-mail: pirogov@appl.sci-nnov.ru

Abstract. Studies of the structure and kinematics of cores associated with the regions of massive star and star cluster formation are necessary for constructing scenario for the evolution of these objects. We analyzed spectral maps of the massive cores of G012.418+00.506, G326.472+00.888, G328.567–00.535, G335.586–00.289 and G343.127–00.063 from the MALT90 survey in the $\text{HCO}^+(1-0)$ and $\text{H}^{13}\text{CO}^+(1-0)$ lines. The cores are at different stages of evolution and have signs of contraction. By fitting spectral maps calculated within the framework of a spherically symmetric model into the observed ones, the parameters of the radial profiles of density, turbulent velocity and contraction velocity were calculated. The power-law index of the density decay with distance from the center varies in the range of $\sim 1.5 - 2.8$. The lowest value is obtained for the core of G326.472+00.888 without internal sources. The contraction velocity in all cores depends weakly on the distance from the center, decreasing with an index of ~ 0.1 , which differs from the free-fall mode. There are indications of rotation for the cores of G328.567–00.535 and G335.586–00.289. Analysis of $^{13}\text{CO}(2-1)$ data from the SEDIGISM survey for the regions G012.418+00.506, G335.586–00.289, and G343.127–00.063 revealed motions from the surrounding gas toward the cores. The results obtained indicate that the massive cores under consideration interact with their environment and are apparently in a state of global collapse.

Keywords: star formation, molecular clouds, dense cores, molecular lines, modeling

1. INTRODUCTION

The scenario for the formation of massive stars ($\gtrsim 8 M_{\odot}$) is under development [1, 2]. Of great importance is the question of the dynamic properties of dense cores where massive stars are formed and the nature of the collapse. Theoretical works considering the collapse of a spherically symmetric core predict various solutions depending on the initial conditions [3]. Thus, a core initially in a state close to equilibrium, with a small influence of external pressure, will slowly evolve in a quasi-stationary regime to a nonequilibrium state. After a protostar is formed in the center of the core, the gas motions in its vicinity will be determined by the free-fall regime with a radial velocity profile $r^{-0.5}$. Over time, the region covered by the collapse increases. The isothermal singular sphere model [4] and the turbulent polytropic sphere model [5], proposed for cores in which massive stars are formed, are examples of quasi-stationary solutions. Nonequilibrium cores, unlike quasi-stationary ones, being in a state of global collapse with a constant velocity of motions directed from the outside inwards [3], will evolve significantly faster. The process of contraction of a nonequilibrium core leads to fragmentation and further growth of central objects, for example, due to the mechanism of competitive accretion [6]. The model of global hierarchical collapse is based on this idea [7]. While the structure and nature of gas motions in the inner region of the core, where free fall occurs, are the same for both models, and the density profiles in the outer regions have the form r^{-2} , it is the systematic velocity profile in the outer regions that can be used to choose between the models.

Estimates of the systematic velocity of gas in the core can be made from an analysis of the observed molecular lines. Thus, an optically thick spectral line formed in a contracting gas becomes asymmetric, and its peak shifts to the “blue” side, which is associated with differences in excitation conditions on the line of sight and the Doppler effect. There is

an analytical method for estimating the contraction velocity on the line of sight from the parameters of the observed line possessing “blue” asymmetry (see, for example, [8]). However, in order to estimate the radial dependence of the contraction velocity in the core, calculations of radiation transfer in the line within a certain model of the core and fitting the calculated spectral map into the observed one are required.

Fitting model spectral maps into observed ones with simultaneous variation of the set of parameters describing the structure and kinematics of the core is a very time-consuming process even for fairly simple spherically symmetric models due to the large number of free parameters, correlations between them and dependence on the initial conditions. To solve this problem, an algorithm based on the use of a pre-calculated array of spectral maps for a fairly wide range of model parameters was developed in [9]. The algorithm uses the principal component (PC) method to reduce the dimensionality of the model and optimally fill the parameter region containing the global minimum of the error function. The k-nearest neighbor (kNN) method is used to find the optimal parameter values corresponding to the minimum.

Among the molecular lines, tracers of dense gas ($\geq 10^5 \text{ cm}^{-3}$), the optically thick lines of the HCO^+ and HCN molecules are the most sensitive to the kinematics and spatial distribution of the density (see, e.g., [10–12]). Using the spherically symmetric model and the above algorithm, we analyzed the spectral maps of the (1–0) transition of the HCO^+ and HCN molecules and their rarer isotopes observed in the core of L1287, in which a star cluster is forming [9], as well as the $\text{HCO}^+(1-0)$ and $\text{H}^{13}\text{CO}^+(1-0)$ maps in the core of G268.42–0.85, associated with the region of formation of a high-mass star [13]. The values of the parameters of the radial profiles of the density and velocity were calculated. For both cores, the calculated radial profiles of the contraction velocity turned out to be different from

those expected in the case of free fall, indicating the preference of the model of an initially nonequilibrium core for these objects.

In order to draw general conclusions about the nature of gas contraction in the cores associated with the regions of formation of massive stars and star clusters, it is necessary to analyze a larger number of objects. For this purpose, objects with signs of contraction were selected from the MALT90 catalog [14]. In this paper, we present estimates of the parameters of the radial profiles of physical parameters, including the systematic velocity, for five MALT90 objects using an algorithm for fitting model spectral maps to observed ones [9]. Section 2 provides brief information about the MALT90 database and the sample of objects. Section 3 describes the objects analyzed in this paper. The results of the analysis of the maps in molecular lines are given in Section 4, their discussion is given in Section 5. The conclusions of the work are formulated in Section 6.

2. SELECTION OF OBJECTS FROM THE MALT90 DATABASE

Surveys of regions of the galactic plane in the continuum at submillimeter waves and in the far infrared range (e.g. ATLASGAL [15], HiGal [16]), as well as in the lines of the CO molecule and its isotopes (e.g., SEDIGISM [17], FUGIN [18]) provide important information on the large-scale distribution of dust and gas. These surveys made it possible to identify the cores of molecular dust clouds associated with the regions of formation of high-mass stars and star clusters. The MALT90 (The Millimetre Astronomy Legacy Team 90 GHz) survey [14, 19], conducted in the direction of massive dust clumps detected by the emission in the continuum at a wavelength of $870 \mu\text{m}$ (ATLASGAL [15]), represents the largest database

of spectroscopic observations of objects of this class.¹ The survey includes observations of more than 2000 objects conducted with the MOPRA-22m radio telescope in the 3-mm wavelength range with an angular resolution of $\sim 36''$. The observations were carried out in 16 spectral subranges. Most of the MALT90 objects are dense cores associated with different stages of the formation of massive stars and star clusters.

As a result of a preliminary analysis of the MALT90 database, we identified 755 objects with noticeable emission in the $\text{HCO}^+(1-0)$ line (peak value $T_a^* \geq 1$ K). In 110 objects, the $\text{HCO}^+(1-0)$ profiles have noticeable asymmetry (the peak is shifted relative to the center of the $\text{H}^{13}\text{CO}^+(1-0)$ and $\text{N}_2\text{H}^+(1-0)$ lines to the “blue” or “red” side) or have a dip, while the intensities of the “blue” and “red” peaks are close. In 20 cores with a dip, the amplitude of the “blue” peak exceeds the amplitude of the “red” one. The presence of asymmetry of this type for optically thick $\text{HCO}^+(1-0)$ lines and symmetric, close to Gaussian, $\text{H}^{13}\text{CO}^+(1-0)$ and $\text{N}_2\text{H}^+(1-0)$ lines, the optical depth of which is significantly lower, and the peak is close to the position of the dip of the $\text{HCO}^+(1-0)$ lines, indicates probable contraction of the core [20]. These objects were selected for further evaluation of physical parameters and analysis of the nature of gas contraction.

This paper presents the results of the analysis of observational data for five of the 20 selected cores at different stages of evolution. The “blue” asymmetry of the $\text{HCO}^+(1-0)$ lines is observed at map scales larger than the radiation pattern ($\geq 1'$). MALT90 data processing consisted of extracting a section with a line from the corresponding spectral subrange, subtracting the 1st–2nd order baseline, and recalculating the intensity scale from the antenna temperature to temperatures reduced to the main beam of the radiation pattern. Since

¹ MALT90 data are publicly available in the Australian Telescope Online Archive (ATOA), <http://atoa.atnf.csiro.au>

the G328.567–00.535 and G328.575–00.527 regions overlapped, they were averaged using the CLASS program from the GILDAS ² package to increase the signal-to-noise ratio. The list of objects is given in Table 1. The names of the objects correspond to the names of the regions from the MALT90 database. Table 1 gives the galactic and equatorial coordinates of the centers of the regions, distances to the objects, their evolutionary status and associations with other objects. Maps of the integrated intensities of HCO⁺(1–0), maps in the continuum according to ATLASGAL data and the infrared maps according to Spitzer data are shown in Fig. 1. The maps also show maser sources and IRAS sources. A detailed description of the objects is given in Section 3.

3. DESCRIPTION OF OBJECTS

The dense core of G012.418+00.506 is associated with the source IRAS 18079–1756, which is likely a massive young stellar object. The core has an outflow [24] and is classified as an extended green object (EGO) [25]. It is associated with an ultracompact H II region [26] and appears to be in a state of global collapse [27]. This core was included in the 6 cm continuum [28] and molecular line [29, 30] surveys, as well as the ATOMS survey conducted in continuum and molecular lines with the ALMA interferometer [27]. The core contains water masers [30–32], as well as methanol masers of classes I [33, 34] and II [35]. ³ The mass of the core according to ATLASGAL data is $414 M_{\odot}$ [37], the temperature of the dust is 25.6 K [21].

The object G326.472+00.888 is a core located near the boundary of the expanding H II region, which was probably formed as a result of compression by a shock wave. The center of

² <http://iram.fr/IRAMFR/GILDAS>

³ Information on the presence of maser sources is taken from the maserdb.net database [36].

the 843 MHz radio emission region [38], as well as the source IRAS 15384–5348, are located at a distance of pc from the center of the core [39]. In addition to ATLASGAL and MALT90 observations, this core was observed in the continuum at 350 μm [40]. We did not find data on the existence of internal sources associated with the core, which may indicate the earliest stage of evolution among the objects in the sample. Observations of maser lines in this core were not carried out. In [21], this object is classified, however, as “PDR+Embedded Source”. The mass of the core according to ATLASGAL data is $\sim 280 M_{\odot}$ [40], the temperature of the dust in the core is ~ 20 K [21, 39, 40].

The core of G328.567–00.535 is associated with an extended H II region [41] and a large-scale bipolar outflow observed in the near and mid-infrared ranges [42]. The core is associated with a cluster of nearinfrared sources [42] and the source IRAS 15557–5337. The evolutionary status according to the classification of the work [21] is “complicated”. In addition to ATLASGAL, the core was included in a survey of massive protostars from the southern hemisphere in molecular lines and in the continuum at 1.2 mm [43]. Observations in the methanol [44] and hydroxyl [45] lines in this core did not give a positive result. The mass of the core according to ATLASGAL data is $\sim 470 M_{\odot}$ [37]. The temperature of the dust in the direction of the core is ~ 35 K [21].

The object G335.586–00.289 is a dark infrared cloud [46] with a hub-filament system, in which, according to the conclusions of [47], a global collapse process is taking place. The IRAS 16272–4837 source is associated with the core. The core was included in a sample of hot cores observed in the continuum at 1.3 mm [48], as well as at 3 mm and 0.87 mm and in the $\text{H}^{13}\text{CO}^+(1-0)$ line with the ALMA interferometer [47]. The evolutionary status according to the classification of [21] is “YSO”. According to the ATLASGAL observations [37], the mass of the core is $\sim 2000 M_{\odot}$ for a distance of 3.8 kpc, which corresponds to $\sim 1700 M_{\odot}$ for the

distance of 3.2 kpc adopted by us. According to the data of [49], however, the mass of the core is significantly higher and is $3.7 \times 10^3 M_{\odot}$. The core contains water [50, 51], hydroxyl [52], and methanol masers of class I [53–55] and class II [56, 57]. The temperature of the dust in the core is ~ 23 K [21].

The core of G343.127–00.063 contains the bright source IRAS 16547–4247 associated with a massive O-type star [58]. The evolutionary status of the core according to the classification of [21] is “H II region”. Interferometric observations in the radio continuum made it possible to detect a thermal jet coming from the center of the core in two opposite directions [59, 60]. According to observations in the CO(3–2) line [58], a collimated bipolar outflow oriented along the radio jet exists in the core. Observations with the ALMA interferometer [61] indicate the existence of a molecular Keplerian disk around the young massive stellar object, the orientation of which is perpendicular to the jet. Maser lines of water [51, 62], hydroxyl [52, 63], and methanol class I [53, 54, 64] are observed in the core. The mass of the core according to ATLASGAL data is $\sim 890 M_{\odot}$ [37], according to observations at 1.2 mm the mass is $\sim 1.3 \times 10^3 M_{\odot}$ [59]. The temperature of the dust in the core is ~ 29 K [21].

The bolometric luminosities of the IRAS sources associated with four cores (except for G326.472+00.888) and calculated as the integral of the fitted “gray” body radiation curve into the frequency dependence of the flux [65] taking into account the distances from Table 1 are $(0.1\text{--}2) \times 10^5 L_{\odot}$. According to our estimates, the source IRAS 15557–5357 has the highest luminosity, and IRAS 18079–1756 has the lowest luminosity.

According to MALT90 data, the following lines were detected in all cores: $\text{HCO}^+(1\text{--}0)$, $\text{N}_2\text{H}^+(1\text{--}0)$, $\text{HCN}(1\text{--}0)$, $\text{HNC}(1\text{--}0)$, $\text{H}^{13}\text{CO}^+(1\text{--}0)$, $\text{HC}_3\text{N}(10\text{--}9)$, and $\text{C}_2\text{H}(1\text{--}0, 3/2\text{--}1/2, \text{F}=2\text{--}1; 3/2\text{--}1/2 \text{F}=1\text{--}0; 1/2\text{--}1/2 \text{F}=1\text{--}1)$. Weak emission was also recorded in the lines $\text{HN}^{13}\text{C}(1\text{--}0)$ and $^{13}\text{CS}(2\text{--}1)$ (G328.567), $\text{HNCO}(4(0,4)\text{--}3(0,3))$ (G335.586) and $\text{SiO}(1\text{--}$

0) (G343.127).⁴ The emission regions in the continuum at 870 μm are close in shape to spherically symmetric (Fig. 1).

To estimate the sizes of the molecular emission regions, a convolution of a two-dimensional Gaussian elliptic function with unknown parameters and a twodimensional circular Gaussian with a width equal to the width of the main beam of the telescope radiation pattern was fitted into the integrated intensity maps [66]. In the core of G012.418, the size of the $\text{HCO}^+(1-0)$ emission region (FWHM), according to our estimates, is ~ 0.5 pc, and the size of the $\text{N}_2\text{H}^+(1-0)$ emission region is ~ 0.4 pc. In the core of G326.472, the shapes of the $\text{HCO}^+(1-0)$ and $\text{N}_2\text{H}^+(1-0)$ emission regions are close to spherically symmetric (Fig. 1), and their sizes are also close and amount to ~ 0.8 pc. The shape of the $\text{HCO}^+(1-0)$ emission region in the core of G328.567 is more elongated compared to the other cores (Fig. 1) (the ratio of the axes of the fitted ellipse is ~ 2) (Fig. 1). The continuum emission region at 870 μm , however, is less elongated (the axial ratio is ~ 1.4 [37]). The $\text{N}_2\text{H}^+(1-0)$ emission peak is shifted relative to $\text{HCO}^+(1-0)$ by ~ 0.5 pc. This fact, as well as significant differences in the sizes of the lines $\text{HCO}^+(1-0)$ (~ 0.8 pc) and $\text{N}_2\text{H}^+(1-0)$ (~ 0.2 pc), indicate chemical differentiation. The shapes of the $\text{HCO}^+(1-0)$ and $\text{N}_2\text{H}^+(1-0)$ emission regions in G335.586 and in G343.127 are close to spherically symmetric (Fig. 1). The sizes of these regions in G335.586 are ~ 0.9 pc and ~ 0.8 pc for $\text{HCO}^+(1-0)$ and $\text{N}_2\text{H}^+(1-0)$, respectively, and pc for both lines in G343.127. Figure 2 shows the spectra of $\text{HCO}^+(1-0)$, $\text{HCN}(1-0)$, $\text{H}^{13}\text{CO}^+(1-0)$ and $\text{N}_2\text{H}^+(1-0)$ in the direction of the integrated intensity peaks of $\text{HCO}^+(1-0)$.

⁴ From here on, abbreviated names of objects are used.

4. ESTIMATION OF PHYSICAL PARAMETERS OF CORES USING MODEL CALCULATIONS

To obtain information on the radial profiles of physical parameters in the cores, including contraction velocity, we fitted model spectral maps into the observed ones. As in [9, 13], we used a multilayer spherically symmetric model of the core (SSL), the parameters of which (density, kinetic temperature, turbulent and systematic velocities) depended only on the radial distance, as $P_0/(1 + (r/R_0)^{\alpha_p})$ (the description of the model is given in the Appendix to the paper [9]). The quantity P_0 is twice the value of the parameter in the central layer with the radius R_0 , which was set equal to 5×10^{-2} pc. The parameters of the model were the values of P_0 for the radial profiles of the density, turbulent and systematic velocities (n_0 , V_{turb} , V_{sys} respectively), and the corresponding power indices (α_n , α_{turb} , α_{sys}), as well as the relative abundances of the HCO^+ and H^{13}CO^+ molecules, which were assumed to be independent of the radial distance. The latter condition can be a fairly rough approximation for the cores of the sample. It is known that even in low-mass prestellar cores, chemical modeling predicts a non-uniform distribution of HCO^+ [67]. However, our calculations using a model in which the HCO^+ abundance varied from the center to the edge by several times did not lead to changes in the estimates of the core parameters that go beyond the confidence ranges. It is likely that when analyzing higher-quality observational data with better angular resolution, taking into account the results of chemical model calculations may be of significant importance.

The kinetic temperature profile for the four cores with internal sources was specified as $60 \text{ K}/(1 + (r/R_0)^{0.3})$ and was not varied. This type of profile corresponds to the dust temperature distribution in the optically thin dust shell surrounding the central source for the dust emissivity value $\beta = 2$ [68, 69] provided that the dust and gas temperature distributions are close. Note that the kinetic temperature distribution in the cores (especially at the

periphery) can be more complex [70, 71]. However, since the $\text{HCO}^+\text{-H}_2$ collision probabilities we used [72] are specified for fixed temperatures with a step of 10 K, the temperatures in the layer were rounded to a value multiple of 10 K, which leveled out possible temperature variations in the outer layers. In accordance with the chosen profile, the kinetic temperature was 30 K in the central layer and dropped to K at the periphery. For the core of G326.472, which apparently has no internal heating source, the kinetic temperature was assumed to be constant at 20 K. After calculating the model spectra, a convolution with the telescope radiation pattern was performed and an error function was calculated that depends on the difference between the model and observed spectra at different points.

In addition to the SSL code, we used the LOC code [73], which uses a deterministic set of rays in Cartesian coordinates to calculate radiative transfer and which is applicable to an arbitrary distribution of parameters in the model cloud, allowing, in particular, to take rotation into account.

The method of applying the algorithm for finding the global minimum of the error function is based on the scheme described in [9, 13]. Since the calculations of the excitation of molecules and the transfer of radiation in lines obviously do not depend on the choice of a specific object and the distance to it, a general library of spectral maps corresponding to a distance to an object of 1 kpc without convolution with the telescope radiation pattern was preliminarily calculated. When analyzing individual sources, the maps were convolved with the telescope radiation pattern and the error function was calculated. For the values of the physical parameters corresponding to the minimum of the error function, the boundaries of the confidence ranges were calculated. To refine the estimates, the Nelder–Mead method and the LOC program were used. In this case, the values calculated from the analysis of the library of spectral maps were taken as initial values. As was shown in [9, 13], the error

function has a single global minimum. When choosing initial values in the vicinity of this minimum, the Nelder–Mead method showed sufficient efficiency and allowed us to estimate the optimal values of the physical parameters when calculating models with a different type of parameterization (with a fixed turbulent velocity profile and taking rotation into account, see Section 5).

The observed and model $\text{HCO}^+(1-0)$ maps of the central regions of the cores are shown in Fig. 3. The values of the physical parameters corresponding to the minimum of the error function, as well as the uncertainties of these estimates, corresponding to the boundaries of the confidence ranges, are given in Table 2.

5. DISCUSSION

The dense MALT90 cores included in the sample represent regions of formation of massive stars at different stages of evolution. The earliest stage of evolution is probably represented by the core G326.472, where there are no indications of the presence of internal sources. However, the widths of optically thin lines in the central regions of this core are higher than at the periphery, indicating an increased degree of dynamical activity in the center (turbulence, systematic motions), which can be associated with the process of star formation. The other four cores are apparently at later stages, as indicated by the presence of high-luminosity IRAS sources, H II zones, maser sources and other sources (see Section 3). Among them, the core of G328.567 stands out, associated with an extended H II zone, a large-scale bipolar outflow and a cluster of infrared sources, where there are no data on the presence of maser sources. The center of the $\text{N}_2\text{H}^+(1-0)$ emission region in this core is shifted relative to the $\text{HCO}^+(1-0)$ center, indicating chemical differentiation, probably associated with the influence of a massive young stellar object. For the remaining cores, the morphologies of the

HCO⁺(1–0) and N₂H⁺(1–0) emission regions, as well as the sizes of their emission regions, are close. The sizes of the emission regions in the HCO⁺(1–0) line vary in the range of 0.4 – 1.0 pc (Section 3). The most compact core is G012.418. The dust temperatures are in the range of $\sim 20 - 35$ K [21]. The core of G328.567 has the highest dust temperature. The masses of the cores calculated from the dust emission in the continuum are in the range from ~ 300 to $\geq 1000 M_{\odot}$ [37, 40]. The core of G335.586 has the largest mass. The virial masses calculated from the H¹³CO⁺(1–0) lines (for G328.567) and N₂H⁺(1–0) (for the remaining cores) are close to the mass estimates calculated from dust, within possible errors, the main contribution to which may apparently be associated with uncertainties in the kinematic distances.

5.1. Analysis of the Results of Model Calculations

By fitting the model maps into the observed maps of HCO⁺(1–0) and H¹³CO⁺(1–0), the parameters of the radial dependences of the density, turbulent velocity, and contraction velocity of the cores were estimated (Table 2). The results of the model calculations describe the observed spectra quite well (Fig. 3). The boundaries of the confidence regions for the parameter values in the center were in some cases strongly asymmetric, which is apparently due to correlations between the parameters and the nonlinear dependence of the error function on the parameters.

The power indices of density decay with distance from the center (α_n) lie in the range $\sim 1.5 - 2.8$. The lowest index was obtained for the core of G326.472, the highest – for the core G335.586. The range of confidence estimates in the latter case, however, is quite large (+0.4/–0.8). The calculated values within the confidence estimates are comparable with the value 1.6 ± 0.3 obtained from observations in the continuum for cores associated with regions

of formation of massive stars and star clusters at different stages of evolution [74]. For four cores with internal sources, the values of the indices α_n , taking into account the confidence ranges, are close to the value of 2 predicted by theoretical models.

The model masses of the cores calculated from the values of the densities at the center (n_0) and the indices α_n (Table 2) turned out, however, to be higher than the estimates calculated from the dust observation data [37, 40], as well as those calculated by us from the C¹⁸O(2–1) observation data [17]. The strongest discrepancy was noted for the cores of G012.418, G326.472 and G328.567 (\geq order of magnitude). For the cores of G335.586 and G343.127, the discrepancies do not go beyond the range of confidence estimates, taking into account the large uncertainties of the n_0 values (Table 2). Also, as a result of the calculations, the turbulent velocity at the center of the cores turns out to be quite high. The highest value was obtained for G343.127, which may be associated with the presence of molecular outflow in this core [58], which is the cause of additional broadening of the HCO⁺(1–0) lines in the center. With increasing distance from the center, the turbulent velocity drops quite sharply with indices of $\sim 0.3 - 0.6$, reaching values of ≤ 1 km/s in the outer layers.

The systematic excess of model masses over independent estimates may indicate a common cause unrelated to errors in parameter estimates. The factor leading to overestimated central densities and, accordingly, masses may be insufficient spatial resolution of observations and probable anisotropic structure of the density and velocity field, unresolved by observations. As shown by interferometric observations of G012.418 and G335.586 [27, 47], the central regions of these cores are highly inhomogeneous. They consist of fragments with different velocities and different line asymmetries. In addition, gas and dust in these regions are concentrated in filaments along which gas motions apparently occur. MALT90 observational data with low angular resolution in this case provide only averaged information on the

radiation coming from these regions, and the use of a spherically symmetric model may lead to a shift in the estimates of the physical parameter values. To a greater extent, these effects can affect the values of the parameters in the center (P_0) and to a lesser extent, the values of the power indices (α_p), determined by the observed spectral maps of the entire core.

To check how the value of the central layer radius affects the obtained results, we performed calculations for $R_0 = 6.5 \times 10^{-3}$ pc. A decrease in R_0 led to a significant increase in the density in the center (by ~ 2 orders of magnitude), to an increase in the turbulent velocity in the center (by $\sim 1.5 - 2$ times) and to a lesser extent led to a change in the values of the systematic velocity and power indices. In particular, the α_{sys} values remained practically unchanged. A check was also performed to what extent a possible overestimation of the turbulent velocity in the center affects the bias in the estimates of other parameters. For this purpose, fixed turbulent velocity profiles calculated from observations of lines with a small optical depth ($N_2H^+(1-0)$ and/or $H^{13}CO^+(1-0)$) were taken for each core. These turbulent velocity profiles had a shape different from that used in the model calculations, changing slightly in the central layers and decreasing to ≤ 1 km/s in the outer layers. In this case, the Nelder–Mead method and the LOC program [73] were used to calculate the values of the remaining parameters. As a result, the central densities n_0 and indices α_n decreased, leading to a decrease in the mass estimates; the values of V_{sys} increased in absolute value, and the values of α_{sys} remained practically unchanged. In Table 2, the values obtained for the case of a fixed turbulent velocity profile are given in each column on the right for comparison.

The contraction velocities in the central layer lie in the range from approximately -0.6 to -1.5 km/s. These values are close to the estimates calculated using the model [8] for the centers of the cores of G328.567, G335.586, and G343.127 based on the parameters of the

observed $\text{HCO}^+(1-0)$ lines, where the dip in the lines is quite pronounced.

5.2. Estimates of the Rotation of the Cores

In some areas of the maps (see Fig. 3), the ratio between the “blue” and “red” peaks of the model spectra differs from the observed ones, which may be caused by rotation. The LOC program was used to estimate the rotation parameters in the cores of G328.567 and G335.586. For the core of G328.567, the $\text{HCO}^+(1-0)$ data were used, and for the core of G335.586, the archived data of APEX-12m observations in the $\text{HCO}^+(3-2)$ line (project C-092.F-9702B-2013) were used, which have a better signal-to-noise ratio than the MALT90 data. The rotation velocity was specified as $V_{rot}(R_0/r)^{\alpha_v}$. The rotation axis was taken to lie in the plane of the sky in the direction of the minimum of the gradient of the first moment map of $\text{HCO}^+(1-0)$. When fitting the model maps to the observed ones, n_0 , V_{sys} , α_n , and α_{sys} were chosen as free parameters, as well as the rotation parameters (V_{rot} and α_v) and the abundance of HCO^+ molecules. The turbulent velocity profile was assumed to be fixed. The optimal rotation parameters were calculated using the Nelder–Mead method and are given in Table 3. The resulting spectral maps are shown in Fig. 4. As a result of the calculations, the error function value decreased by 20% for G328.567 and by 50% for G335.586. For the core of G328.567, the index α_v turned out to be close to 0.4, which may indicate a rotation law close to the Keplerian one. Taking into account the rotation in this core led to a significant decrease in the estimate of V_{sys} (cf. the corresponding values from Table 2, right column, and from Table 3). The power index of the radial contraction velocity profile did not change. For G335.586, the rotation velocity depends weakly on the radial distance. This region may be at an earlier stage of evolution compared to G328.567, where there is a large-scale bipolar outflow and, probably, a disk structure. This conclusion is consistent

with the results of model calculations from [75], which show that the primary disk at an early stage of evolution can rotate according to a law close to a solid state. An alternative explanation for the variations in the line asymmetry in the core of G335.586 may be the anisotropic nature of accretion associated with gas flows along the filaments [76]. To obtain more definitive conclusions, further observational studies of this core should be carried out, which will allow us to estimate its kinematics as a whole.

5.3. *Velocity Profiles in the Gas Surrounding the Cores*

One of the results of our analysis was that the contraction velocities of the cores are practically independent of the radial distance. This fact may be related to the fact that the cores are not isolated objects, but are in a state of global contraction, and gas is probably supplied to them from the surrounding gas. To search for indications of the existence of such processes, it is necessary to analyze the kinematics of the surrounding gas based on observations in lines excited at lower densities and on scales exceeding the scale of the cores.

Three cores from our sample (G012.418+00.506, G335.586-00.289, and G343.127-00.063) were observed in the SEDIGISM survey in the $^{13}\text{CO}(2-1)$ and $\text{C}^{18}\text{O}(2-1)$ lines.⁵ The $^{13}\text{CO}(2-1)$ line is an indicator of gas with a lower density than $\text{HCO}^+(1-0)$ ($\sim 10^4 \text{ cm}^{-3}$). Figure 5 shows maps of the regions containing the cores in the $^{13}\text{CO}(2-1)$ line (left panels), the velocity profiles calculated from the $^{13}\text{CO}(2-1)$ lines, and the integrated intensity profiles (right panels). The maps mark the positions for which the $^{13}\text{CO}(2-1)$ line velocities were calculated. The $^{13}\text{CO}(2-1)$ line velocities are in most cases close to the corresponding velocities of the optically thin $\text{C}^{18}\text{O}(2-1)$ lines. It turned out that in all cases a decrease

⁵ The SEDIGISM database (<https://sedigism.mpifrbonn.mpg.de/index.html>) was created by James Urquhart and is maintained by the Max Planck Institute for Radio Astronomy.

in velocity (down to $\gtrsim 1$ km/s) is observed in the direction of the cores compared to the velocities of the surrounding gas (the “V”-type velocity profile). This may be due to flows of the surrounding gas toward the core located on the line of sight closer to the observer (see, for example, [77, 78]). The right panels of Fig. 5 show with smooth curves the results of fitting into the observations data the projections of the radial profile of the gas velocity in the filament along which the flow is directed: $V(L) = V_{LSR} - V_{sys}(L) \cos A$ (see, for example, [77]). In the given formula, $L = r \sin A$ is the projection of the radial distance r onto the plane of the sky, A is the angle between the direction of the radial gas motions and the line of sight. The radial velocity profile was specified as $V_{sys} \propto r^{-\alpha}$. The curves correspond to three different values of α . The model profiles for $\alpha \lesssim 0.5$ for all three cores describe the data better compared to $\alpha = 1$, while the model with $\alpha = 0.1$ has a slightly smaller residual and, thus, may be preferable compared to $\alpha = 0.5$. The analysis of the velocity profiles constructed in the directions perpendicular to those shown in Fig. 5 did not reveal any “V”-type features for G012.418 and G335.586, which indicates an anisotropic nature of the gas movements from the outside to these cores. In the core of G343.127, such a feature is also noted along the perpendicular direction; the gas flows here may be more isotropic.

Summarizing the obtained results, we note that for all five massive cores associated with the regions of formation of massive stars at different stages of evolution, the power-law index of the radial profile of the contraction velocity turned out to be practically flat, differing from the value of 0.5 corresponding to the regime of free fall of gas onto the protostar. The velocity profiles in the surrounding gas of lower density, calculated from the $^{13}\text{CO}(2-1)$ data in the cores of G012.418, G335.586 and G343.127, indicate the existence of flows, the velocity profiles of which have indices $\lesssim 0.5$. Apparently, the cores are nonequilibrium and interact with the surrounding gas. This is consistent with the conclusions of [27, 47] on the global

collapse of the cores of G012.418 and G335.586. For these cores, flows from the outside apparently occur along large-scale filaments, while for the core of G343.127 the inflow of gas from the outside can be carried out relatively isotropically. Thus, the obtained results correspond to theoretical models considering cores as nonequilibrium objects in a state of global collapse (see, for example, [3, 7]). To confirm the obtained conclusions about the kinematics of gas in cores and the gas surrounding them, as well as to obtain more rigorous estimates of physical parameters, further studies are needed on various scales of both already studied cores and new objects associated with regions of formation of massive stars, with better angular resolution and better sensitivity.

6. CONCLUSIONS

In order to study the characteristics of contracting massive cores, we analyzed the spectral observation data of the objects G012.418+00.506, G326.472+00.888, G328.567–00.535, G335.586–00.289, and G343.127–00.063 from the MALT90 database. The objects have dense cores associated with regions of formation of massive stars at different stages of evolution. The core of G326.472+00.888, for which there are no indications of the existence of internal sources, is apparently at the earliest stage of evolution compared to the others. Optically thick $\text{HCO}^+(1-0)$ lines in all cores exhibit a “blue” asymmetry and a dip, while lines with smaller optical depth ($\text{H}^{13}\text{CO}^+(1-0)$, $\text{N}_2\text{H}^+(1-0)$) are relatively symmetrical, which may indicate contraction.

Data analysis by fitting spectral maps calculated within the spherically symmetric model of the core into the observed maps using the error function minimization algorithm [9] allowed us to calculate the optimal values of the parameters of the radial density, turbulent velocity, and contraction velocity profiles in the cores. The power-law index of density decay with

distance from the center varies in the range , the lowest value of the index was obtained for the core G326.472+00.888. The turbulent velocity decreases with the index $\sim 0.3-0.6$. The contraction velocity of the cores depends weakly on the distance from the center, the power-law index of contraction velocity decay with distance from the center was ~ 0.1 for all cores, which differs from the value of 0.5 for the free fall mode. In the cores of G328.567-00.535 and G335.586-00.289, in addition to radial motions, there are indications of rotation. For G328.567-00.535, the rotation law is close to Keplerian, for G335.586-00.289 the rotation velocity profile is close to flat.

Using the $^{13}\text{CO}(2-1)$ data from the SEDIGISM survey, velocity profiles were plotted for the three regions. In the direction of the cores, “V”-type features were found that may be associated with gas flows onto the core. Fitting the projections of the function of the form $r^{-\alpha}$ into the obtained diagrams indicates the preference of profiles with indices $\alpha \lesssim 0.5$.

The results obtained indicate that the massive cores under consideration interact with their environment and are apparently in a state of global collapse.

REFERENCES

1. J. C. Tan, M. T. Beltran, P. Caselli, F. Fontani, A. Fuente, M. R. Krumholz, C. F. McKee, and A. Stolte, in *Protostars and Planets VI*, Ed. by H. Beuther, R. S. Klessen, C. P. Dullemond, and T. Henning (Univ. Arizona Press, Tucson, 2014), p. 149.
2. F. Motte, S. Bontemps, and F. Louvet, *Ann. Rev. Astron. Astrophys.* 56, 41 (2018).
3. A. Whitworth and D. Summers, *Mon. Not. R. Astron. Soc.* 214, 1 (1985).
4. F. H. Shu, *Astrophys. J.* 214, 488 (1977).
5. C. F. McKee and J. C. Tan, *Astrophys. J.* 585, 850 (2003).
6. I. A. Bonnell, M. R. Bate, C. J. Clarke, and J. E. Pringle, *Mon. Not. R. Astron. Soc.* 323, 785 (2001).
7. E. Vazquez-Semadeni, A. Palau, J. Ballesteros-Paredes, G. C. Gomez, and M. Zamora-Aviles, *Mon. Not. R. Astron. Soc.* 490, 3061 (2019).
8. P. C. Myers, D. Mardones, M. Tafalla, J. P. Williams, and D. J. Wilner, *Astrophys. J. Lett.* 465, L133 (1996).
9. L. E. Pirogov and P. M. Zemlyanukha, *Astron. Rep.* 65, 82 (2021).
10. Y.-X. He, J.-J. Zhou, J. Esimbek, W.-G. Ji, et al., *Mon. Not. R. Astron. Soc.* 461, 2288 (2016).
11. L. E. Pirogov, V. M. Shul'ga, I. I. Zinchenko, P. M. Zemlyanukha, A. H. Patoka, and M. Tomasson, *Astron. Rep.* 60, 904 (2016).
12. H. Yoo, K.-T. Kim, J. Cho, M. Choi, J. Wu, N. J. Evans II, and L. M. Ziurys, *Astrophys. J. Suppl.* 235, 31 (2018).
13. L. E. Pirogov, P. M. Zemlyanukha, E. M. Dombek, and M. A. Voronkov, *Astron. Rep.* 67, 1355 (2023).
14. J. M. Jackson, J. M. Rathborne, J. B. Foster, J. S. Whitaker, et al., *Publ. Astron.*

Soc. Austral. 30, e057 (2013).

15. F. Schuller, K. M. Menten, Y. Contreras, F. Wyrowski, et al., *Astron. Astrophys.* 504, 415 (2009).

16. S. Molinari, B. Swinyard, J. Bally, M. Barlow, et al., *Publ. Astron. Soc. Pacif.* 122 (889), 314 (2010).

17. F. Schuller, J. S. Urquhart, T. Csengeri, D. Colombo, et al., *Mon. Not. R. Astron. Soc.* 500, 3064 (2021).

18. T. Umemoto, T. Minamidani, N. Kuno, S. Fujita, et al., *Publ. Astron. Soc. Jpn.* 69, 78 (2017).

19. J. M. Rathborne, J. S. Whitaker, J. M. Jackson, J. B. Foster, et al., *Publ. Astron. Soc. Austral.* 33, e030 (2016).

20. N. J. Evans II, *Ann. Rev. Astron. Astrophys.* 37, 311 (1999).

21. J. S. Urquhart, M. R. A. Wells, T. Pillai, S. Leurini, et al., *Mon. Not. R. Astron. Soc.* 510, 3389 (2022).

22. A. E. Guzman, P. Sanhueza, Y. Contreras, H. A. Smith, J. M. Jackson, S. Hoq, and J. M. Rathborne, *Astrophys. J.* 815, 130 (2015).

23. Galactic Legacy Infrared Midplane Survey Extraordinaire (GLIMPSE).
<https://irsa.ipac.caltech.edu/data/SPITZER/GLIMPSE/>.

24. N. Issac, A. Tej, T. Liu, W. Varricatt, S. Vig, C. H. Ishwara Chandra, and M. Schultheis, *Mon. Not. R. Astron. Soc.* 485, 1775 (2019).

25. C. J. Cyganowski, B. A. Whitney, E. Holden, E. Braden, et al., *Astron. J.* 136, 2391 (2008).

26. X. Chen, Z.-Q. Shen, J.-J. Li, Y. Xu, and J.-H. He, *Astrophys. J.* 710, 150 (2010).

27. A. Saha, A. Tej, H.-L. Liu, T. Liu, et al., *Mon. Not. R. Astron. Soc.* 516, 1983

(2022).

28. J. S. Urquhart, M. G. Hoare, C. R. Purcell, S. L. Lumsden, et al., *Astron. Astrophys.* 501, 539 (2009).

29. Y. L. Shirley, N. J. Evans II, K. E. Young, C. Knez, and D. T. Jaffe, *Astrophys. J. Suppl.* 149, 375 (2003).

30. C. J. Cyganowski, J. Koda, E. Rosolowsky, S. Towers, J. Donovan Meyer, F. Egusa, R. Momose, and T. P. Robitaille, *Astrophys. J.* 764, 61 (2013).

31. R. Cesaroni, F. Palagi, M. Felli, M. Catarzi, G. Comoretto, S. di Franco, C. Giovannardi, and F. Palla, *Astron. Astrophys. Suppl. Ser.* 76, 445 (1988). 32. B. E. Svoboda, Y. L. Shirley, C. Battersby, E. W. Rosolowsky, et al., *Astrophys. J.* 822, 59 (2016).

33. X. Chen, S. P. Ellingsen, Z.-Q. Shen, A. Titmarsh, and C.-G. Gan, *Astrophys. J. Suppl.* 196, 9 (2011).

34. W. Yang, Y. Xu, X. Chen, S. P. Ellingsen, D. Lu, B. Ju, and Y. Li, *Astrophys. J. Suppl.* 231, 20 (2017).

35. H. Nguyen, M. R. Rugel, C. Murugesan, K. M. Menten, et al., *Astron. Astrophys.* 666, A59 (2022).

36. D. A. Ladeyschikov, O. S. Bayandina, and A. M. Sobolev, *Astron. J.* 158, 233 (2019).

37. T. Csengeri, S. Bontemps, F. Wyrowski, S. T. Megeath, F. Motte, A. Sanna, M. Wienen, and K. M. Menten, *Astron. Astrophys.* 601, A60 (2017).

38. T. Mauch, T. Murphy, H. J. Buttery, J. Curran, R. W. Hunstead, B. Piestrzynski, J. G. Robertson, and E. M. Sadler, *Mon. Not. R. Astron. Soc.* 342, 1117 (2003).

39. N.-P. Yu, J.-L. Xu, J.-J. Wang, and X.-L. Liu, *Astrophys. J.* 865, 135 (2018).

40. Y. Lin, T. Csengeri, F. Wyrowski, J. S. Urquhart, F. Schuller, A. Weiss, and K. M. Menten, *Astron. Astrophys.* 631, A72 (2019).

41. T. Culverhouse, P. Ade, J. Bock, M. Bowden, et al., *Astrophys. J. Suppl.* 195, 8 (2011).
42. J. P. Phillips and J. A. Perez-Grana, *Mon. Not. R. Astron. Soc.* 393, 354 (2009).
43. F. Fontani, M. T. Beltran, J. Brand, R. Cesaroni, L. Testi, S. Molinari, and C. M. Walmsley, *Astron. Astrophys.* 432, 921 (2005).
44. G. C. MacLeod, D. J. van der Walt, A. North, M. J. Gaylard, J. A. Galt, and G. H. Moriarty-Schieven, *Astron. J.* 116, 2936 (1998).
45. R. J. Cohen, M. R. W. Mashedier, and J. L. Caswell, *Mon. Not. R. Astron. Soc.* 274, 808 (1995).
46. N. Peretto and G. A. Fuller, *Astron. Astrophys.* 505, 405 (2009).
47. F.-W. Xu, K. Wang, T. Liu, P. F. Goldsmith, et al., *Mon. Not. R. Astron. Soc.* 520, 3259 (2023).
48. K. Ishihara, P. Sanhueza, F. Nakamura, M. Saito, et al., arXiv: 2407.06845 [astro-ph.GA] (2024).
49. M. Anderson, N. Peretto, S. E. Ragan, A. J. Rigby, et al., *Mon. Not. R. Astron. Soc.* 508, 2964 (2021).
50. A. J. Walsh, C. R. Purcell, S. N. Longmore, S. L. Breen, J. A. Green, L. Harvey-Smith, C. H. Jordan, and C. Macpherson, *Mon. Not. R. Astron. Soc.* 442, 2240 (2014).
51. S. L. Breen, J. L. Caswell, S. P. Ellingsen, and C. J. Phillips, *Mon. Not. R. Astron. Soc.* 406, 1487 (2010).
52. J. L. Caswell, J. A. Green, and C. J. Phillips, *Mon. Not. R. Astron. Soc.* 439, 1680 (2014).
53. M. A. Voronkov, J. L. Caswell, S. P. Ellingsen, J. A. Green, and S. L. Breen, *Mon. Not. R. Astron. Soc.* 439, 2584 (2014).

54. S. L. Breen, Y. Contreras, J. R. Dawson, S. P. Ellingsen, M. A. Voronkov, and T. P. McCarthy, *Mon. Not. R. Astron. Soc.* 484, 5072 (2019).
55. X. Chen, S. P. Ellingsen, Z.-Q. Shen, A. Titmarsh, and C.-G. Gan, *Astrophys. J. Suppl.* 196, 9 (2011).
56. A. J. Walsh, M. G. Burton, A. R. Hyland, and G. Robinson, *Mon. Not. R. Astron. Soc.* 301, 640 (1998).
57. J. L. Caswell, *Publ. Astron. Soc. Austral.* 26, 454 (2009).
58. G. Garay, D. Mardones, L. Bronfman, K. J. Brooks, et al., *Astron. Astrophys.* 463, 217 (2007).
59. G. Garay, K. J. Brooks, D. Mardones, and R. P. Norris, *Astrophys. J.* 587, 739 (2003).
60. L. F. Rodriguez, G. Garay, K. J. Brooks, and D. Mardones, *Astrophys. J.* 626, 953 (2005).
61. L. A. Zapata, G. Garay, A. Palau, L. F. Rodriguez, M. Fernandez-Lopez, R. Estalella, and A. Guzman, *Astrophys. J.* 872, 176 (2019).
62. J. R. Forster and J. L. Caswell, *Astron. Astrophys. Suppl. Ser.* 137, 43 (1999).
63. H.-H. Qiao, A. J. Walsh, J. A. Green, S. L. Breen, et al., *Astrophys. J. Suppl.* 227 (2), 26 (2016).
64. V. I. Slysh, S. V. Kalenskii, I. E. Valts, and R. Otrupcek, *Mon. Not. R. Astron. Soc.* 268, 464 (1994).
65. L. Pirogov, I. Zinchenko, P. Caselli, and L. E. B. Johansson, *Astron. Astrophys.* 461, 523 (2007).
66. L. Pirogov, I. Zinchenko, P. Caselli, L. E. B. Johansson, and P. C. Myers, *Astron. Astrophys.* 405, 639 (2003).

67. Y. Pavlyuchenkov, D. Wiebe, R. Launhardt, and T. Henning, *Astrophys. J.* 645, 1212 (2006).
68. S. Terebey, C. J. Chandler, and P. Andre, *Astrophys. J.* 414, 759 (1993).
69. S. D. Doty and C. M. Leung, *Astrophys. J.* 424, 729 (1994).
70. Y. N. Pavlyuchenkov, D. S. Wiebe, A. M. Fateeva, and T. S. Vasyunina, *Astron. Rep.* 55, 1 (2011).
71. Y. N. Pavlyuchenkov, A. G. Zhilkin, E. I. Vorobyov, and A. M. Fateeva, *Astron. Rep.* 59, 133 (2015).
72. D. R. Flower, *Mon. Not. R. Astron. Soc.* 305, 651 (1999).
73. M. Juvella, *Astron. Astrophys.* 644, A151 (2020).
74. L. E. Pirogov, *Astron. Rep.* 53, 1127 (2009).
75. S. A. Khaibrakhmanov, A. E. Dudorov, N. S. Kargaltseva, and A. G. Zhilkin, *Astron. Rep.* 65, 693 (2021).
76. M. R. A. Wells, H. Beuther, S. Molinari, P. Schilke, et al., *Astron. Astrophys.* 690, A185 (2024).
77. A. Hacar, J. Alves, M. Tafalla, and J. R. Goicoechea, *Astron. Astrophys.* 602, L2 (2017).
78. J. W. Zhou, F. Wyrowski, S. Neupane, J. S. Urquhart, et al., *Astron. Astrophys.* 676, A69 (2023).

Translated by T. Sokolova

Table 1. List from cores from the MALT90 database

Object	l (deg)	b (deg)	$\alpha(2000)$ (hh:mm:ss)	$\delta(2000)$ ($^{\circ}$:':")	D (kpc)	Evolutionary status	Associations with other objects
G012.418+00.506	12.419	0.507	18:10:51.1	-17:55:49.6	1.8	H	IRAS 18079-1756, SIRDC
G326.472+00.888	326.472	0.889	15:42:29.6	-53:58:26.7	2.5	U	
G328.567-00.535	328.568	-0.534	15:59:37.4	-53:45:51.7	2.9	H	IRAS 15557-5337, RCW99
G335.586-00.289	335.586	-0.289	16:30:58.7	-48:43:48.0	3.2	A	IRAS 16272-4837, SIRDC_335.579-0.292
G343.127-00.063	343.128	-0.063	16:58:17.5	-42:52:04.0	2.8	A	IRAS 16547-4247, SIRDC , EGO

Kinematic distances to objects are taken from the survey [21]. The evolutionary status of cores according to the data of [19, 22] is as follows: H – H II region, A – protostellar core, U – status not determined.

Table 2. Model values of physical parameters of cores

Parameter	G012.418+00.506		G326.472+00.888		G328.567-00.535		G335.586-00.289		G343.127-00.063	
$\log(n_0)$	$7.3^{+0.1}_{-1.1}$	7.2	$7.3^{+0.7}_{-0.4}$	6.7	$7.9^{+0.1}_{-0.6}$	7.4	$8.0^{+0.2}_{-1.0}$	7.8	$7.0^{+0.8}_{-0.2}$	6.4
α_n	$2.3^{+0.1}_{-0.2}$	1.5	$1.5^{+0.3}_{-0.1}$	1.2	$1.8^{+0.1}_{-0.5}$	1.5	$2.8^{+0.4}_{-0.8}$	2.5	$2.0^{+0.3}_{-0.2}$	1.8
V_{turb} (km/s)	$3.7^{+1.4}_{-0.2}$		$10.4^{+3.7}_{-1.1}$		$6.8^{+6.8}_{-1.4}$		$5.0^{+2.9}_{-1.8}$		$17.3^{+0.2}_{-5.8}$	
α_{turb}	$0.3^{+0.02}_{-0.1}$		$0.5^{+0.1}_{-0.08}$		$0.35^{+0.23}_{-0.08}$		$0.30^{+0.2}_{-0.05}$		$0.6^{+0.01}_{-0.14}$	
V_{sys} (km/s)	$-2.5^{+0.9}_{-0.7}$	-1.9	$-2.3^{+0.5}_{-0.4}$	-5.5	$-1.1^{+0.1}_{-1.1}$	-3.5	$-2.1^{+0.7}_{-0.6}$	-2.7	$-3.0^{+0.3}_{-2.5}$	-3.2
α_{sys}	$0.12^{+0.06}_{-0.06}$	0.0	$0.13^{+0.07}_{-0.09}$	0.09	$0.06^{+0.14}_{-0.03}$	0.0	$0.11^{+0.11}_{-0.06}$	0.1	$0.07^{+0.1}_{-0.07}$	0.09
$\log X(\text{HCO}^+)$	$-10.2^{+0.3}_{-0.7}$	-10.7	$-10.9^{+0.4}_{-0.4}$	-10.8	$-10.8^{+0.3}_{-1.1}$	-10.8	$-9.6^{+0.2}_{-0.6}$	-10.0	$-9.6^{+0.3}_{-0.7}$	-9.2

n_0 , V_{turb} and V_{sys} represent doubled values of the parameters in the central layer with the radius $R_0 = 5 \times 10^{-2}$ pc; n_0 has the dimension [cm^{-3}]. On the right in each column for a given object are the results of calculations with a fixed turbulent velocity profile (see text).

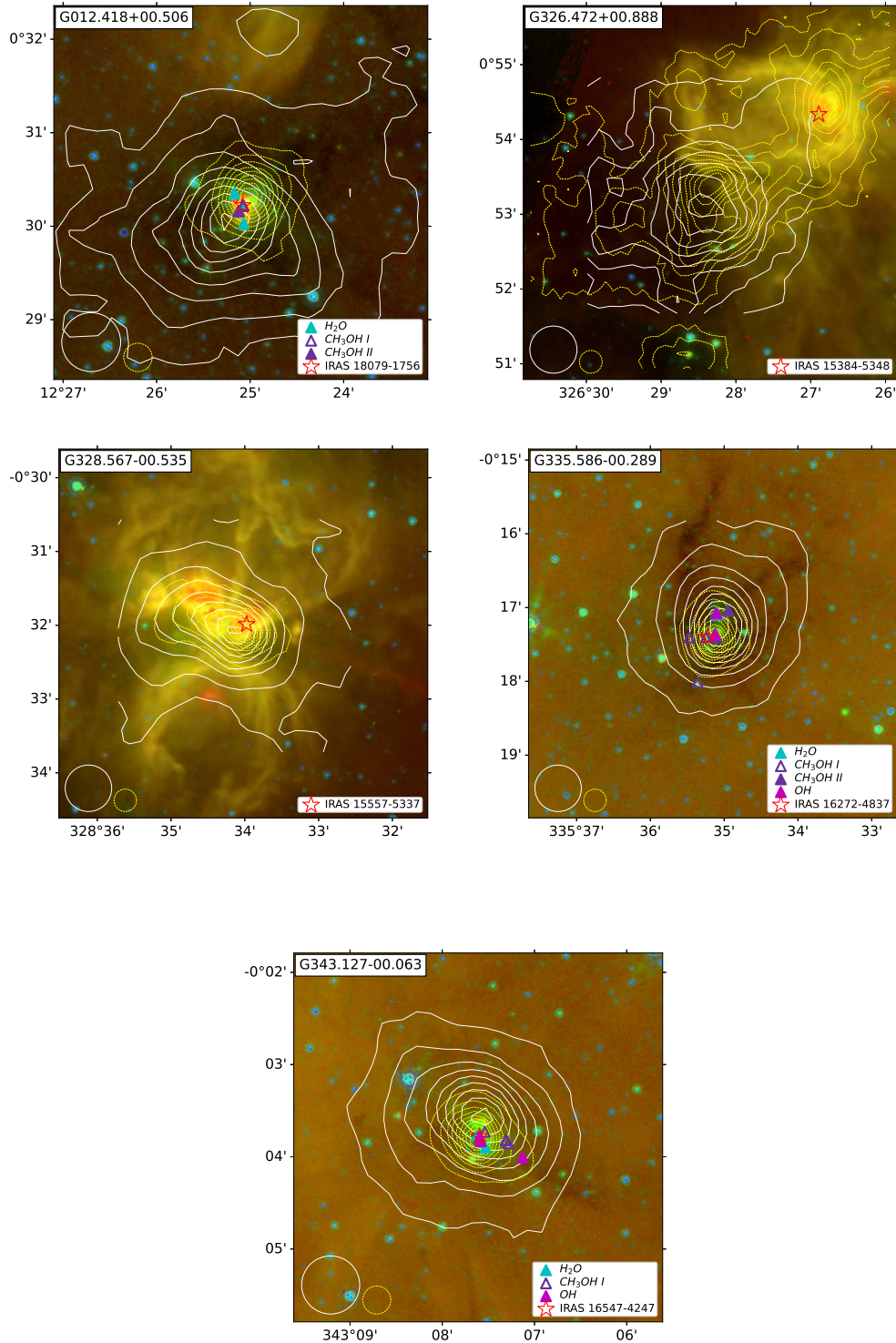


Figure 1. Maps of the MALT90 cores in Galactic coordinates. Spitzer data are shown in colors: 8 μm (red), 5.8 μm (green), and 3.6 μm (blue) [23]. Yellow dashed contours represent the 870 μm ATLASGAL data [15]. The $\text{HCO}^+(1-0)$ integrated intensity contours are shown in white. The contours vary from 10% to 90% of the peak values which are equal to 7.3, 3.4, 12.5, 12.1, and 18.9 Jy/beam (ATLASGAL) and 27.8, 21.5, 32.0, 42.8, and 39.0 K km/s (HCO^+) for G012.418, G326.472, G328.567, G335.586, and G343.127, respectively. The IRAS and maser source positions as well as the main beams of MOPRA-22m (36'' at 86 GHz) and APEX-12m (19'' at 345 GHz) are also shown.

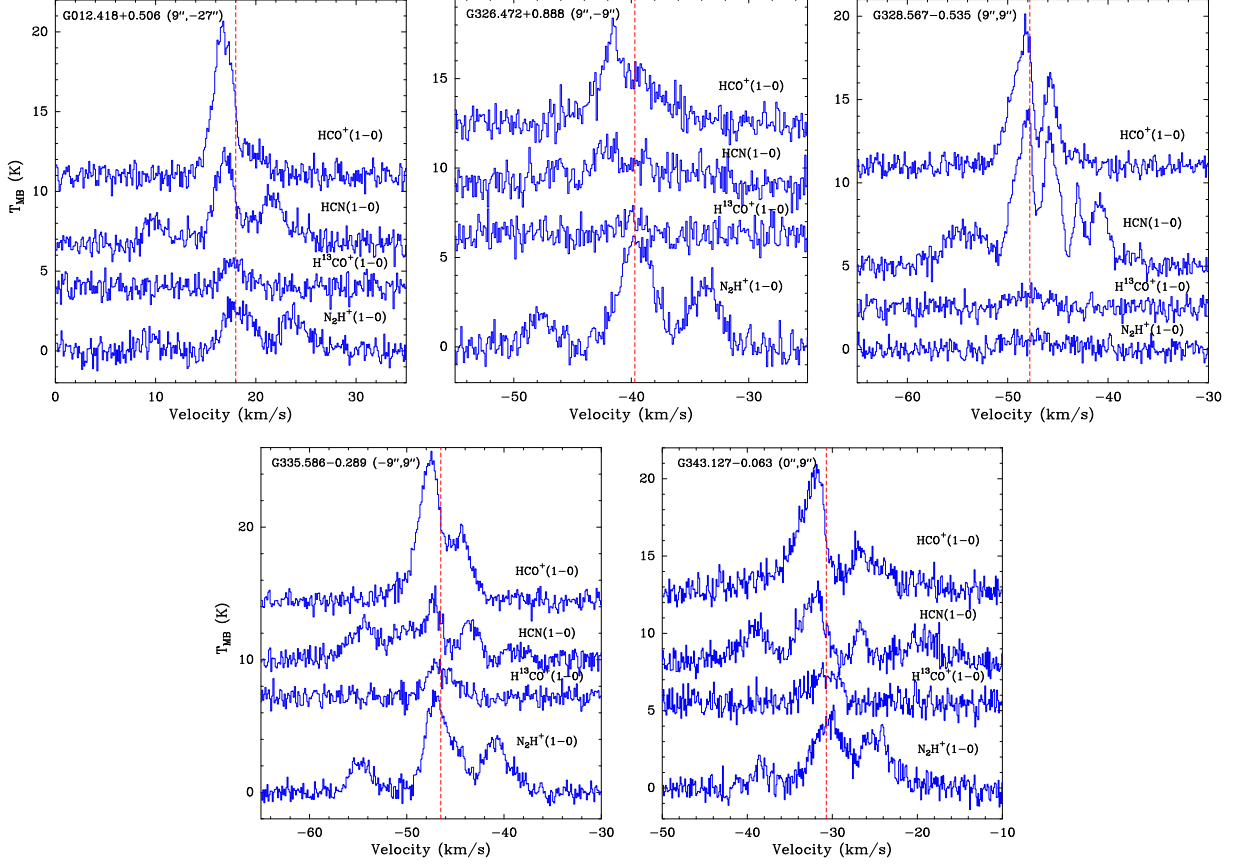


Figure 2. Spectra in the direction of emission peaks in the cores from the sample. Each figure shows the name of the core and its position on the map (shift relative to the coordinates given in Table 1). The horizontal axes show the radial velocity, and the vertical axes show the intensity in units of temperature reduced to the main beam of the telescope (T_{MB}). The vertical dashed red lines correspond to the centers of optically thin $\text{H}^{13}\text{CO}^+(1-0)$ lines, which coincide with the centers of the $\text{N}_2\text{H}^+(1-0)$ lines in all cores except G335.586.

Table 3. Model values of physical parameters of cores taking into account rotation

Parameter	G328.567-00.535	G335.586-00.289
$\log(n_0)$	7.8	6.7
α_n	1.9	2.2
V_{sys} (km/s)	-0.8	-2.7
α_{sys}	0.0	0.1
V_{rot} (km/s)	2.3	0.8
α_v	0.4	0.1
$\log X(\text{HCO}^+)$	-10.5	-9.0

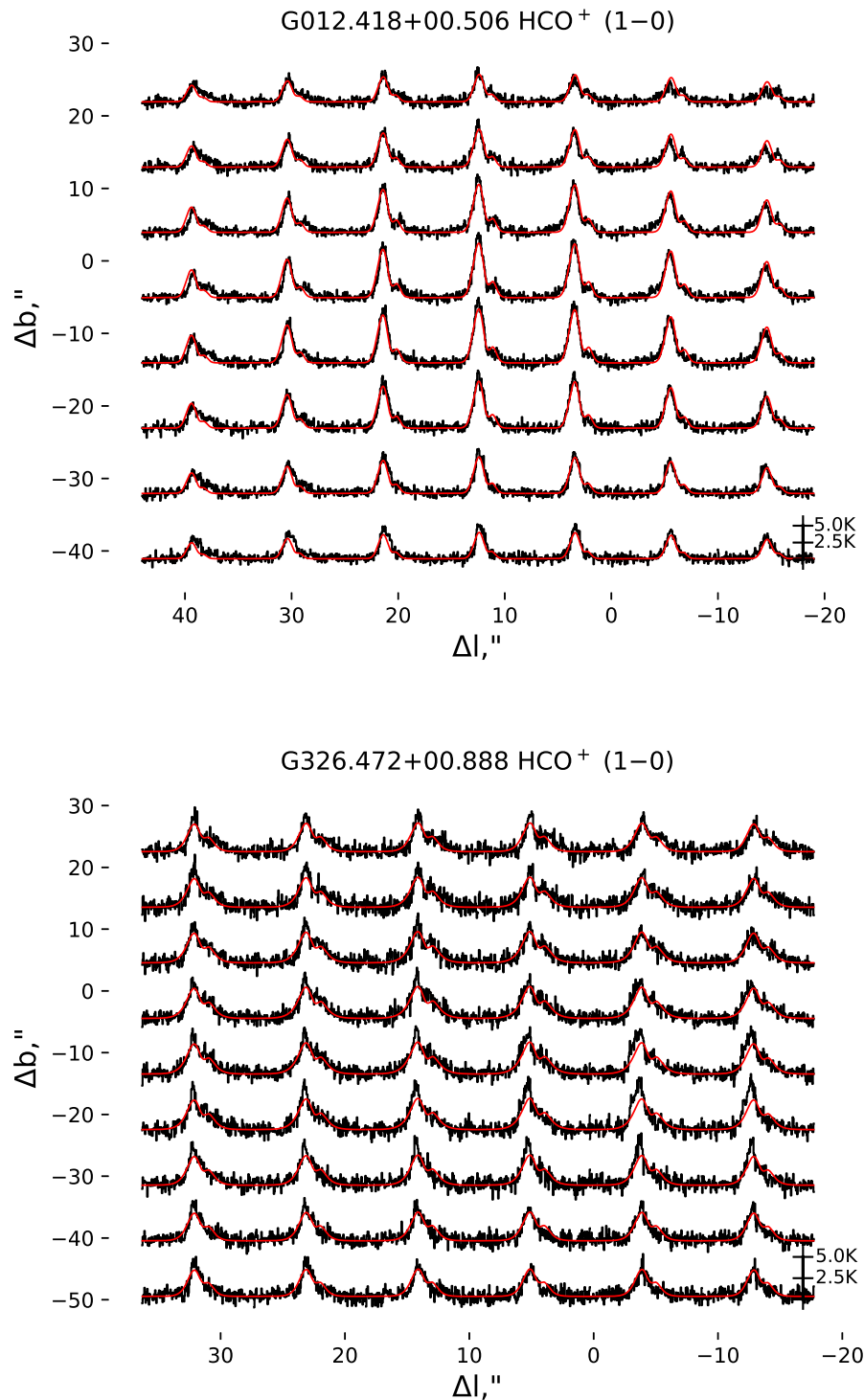


Figure 3. Observed (black) and model (red) HCO⁺(1-0) maps of the cores. The axes are the offsets relative to the coordinates given in Table 1. The intensity scale is indicated in the lower right corner of each figure. Velocity varies from 7 to 26 km/s, from -52 to -29 km/s, from -65 to -30 km/s, from -54 to -39 km/s, and from -42 to -20 km/s for G012.418, G326.472, G328.567; G335.586 and G343.127, respectively.

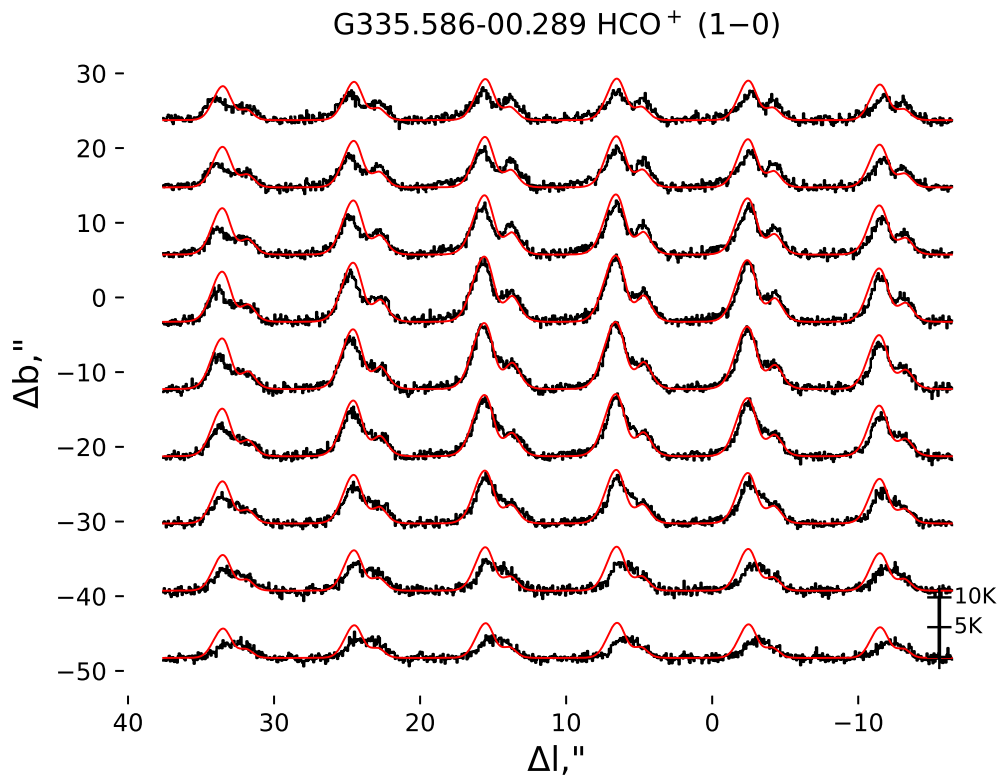
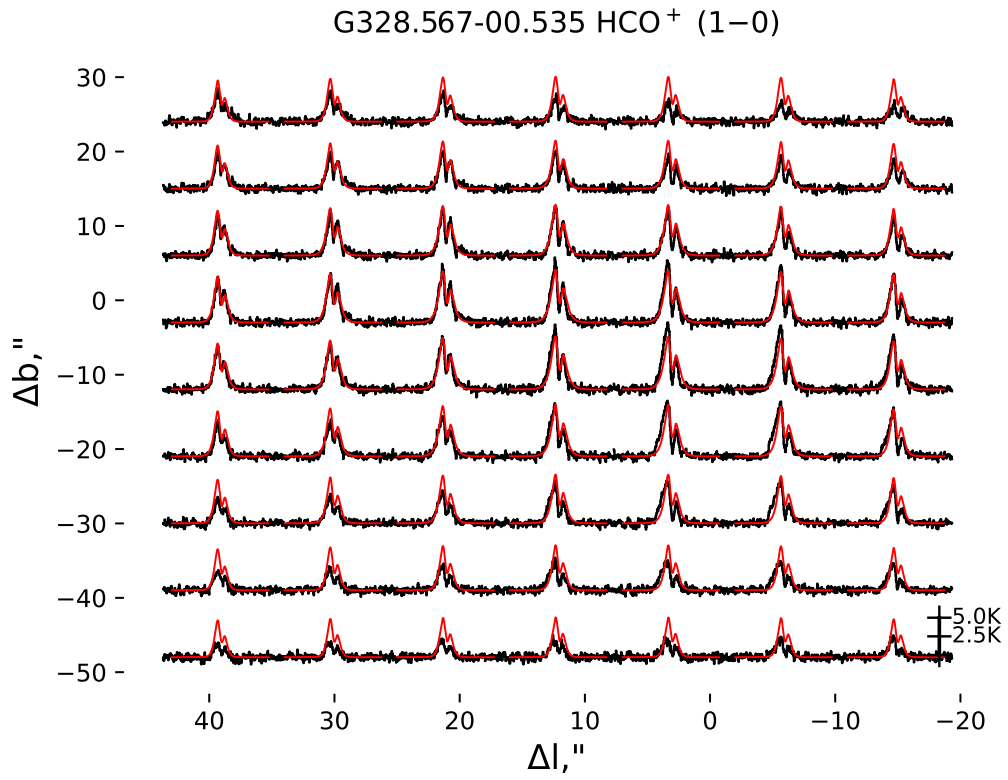


Figure 3. Continued

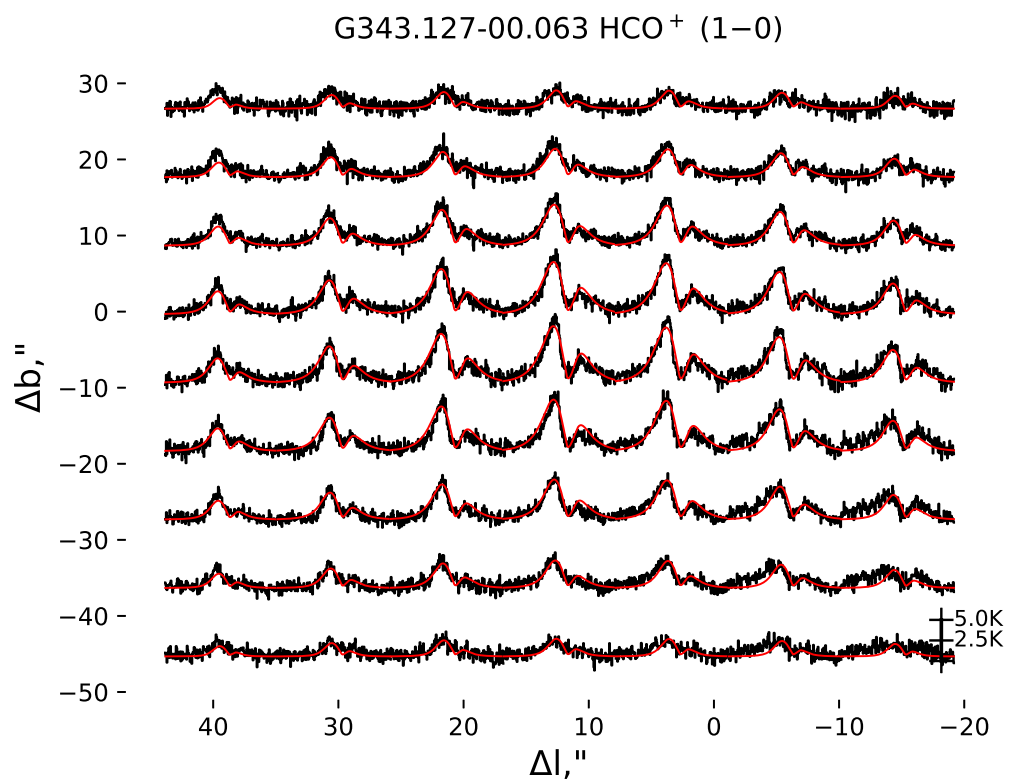


Figure 3. Continued

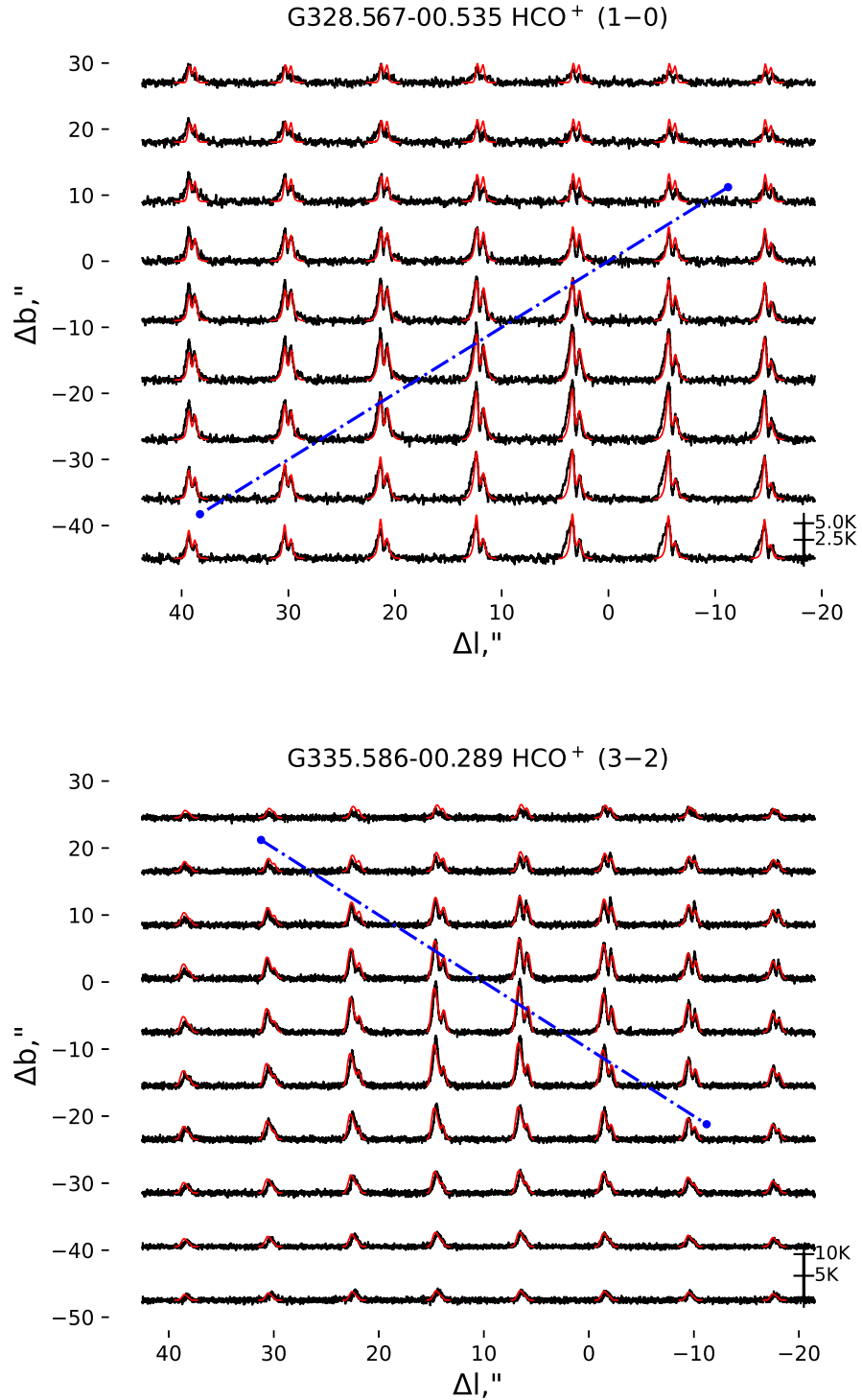


Figure 4. Observed (black) and model (red) (1-0) and (3-2) HCO⁺ maps of G328.567 and G335.586, respectively. The velocity varies from -65 to -30 km/s and from -55 to -35 km/s for G328.567 and G335.586, respectively. Here, the model with radial and rotational motions is used. The blue lines show the rotation axes. Above the axes, the rotational motions are directed toward the observer, below them, away from the observer.

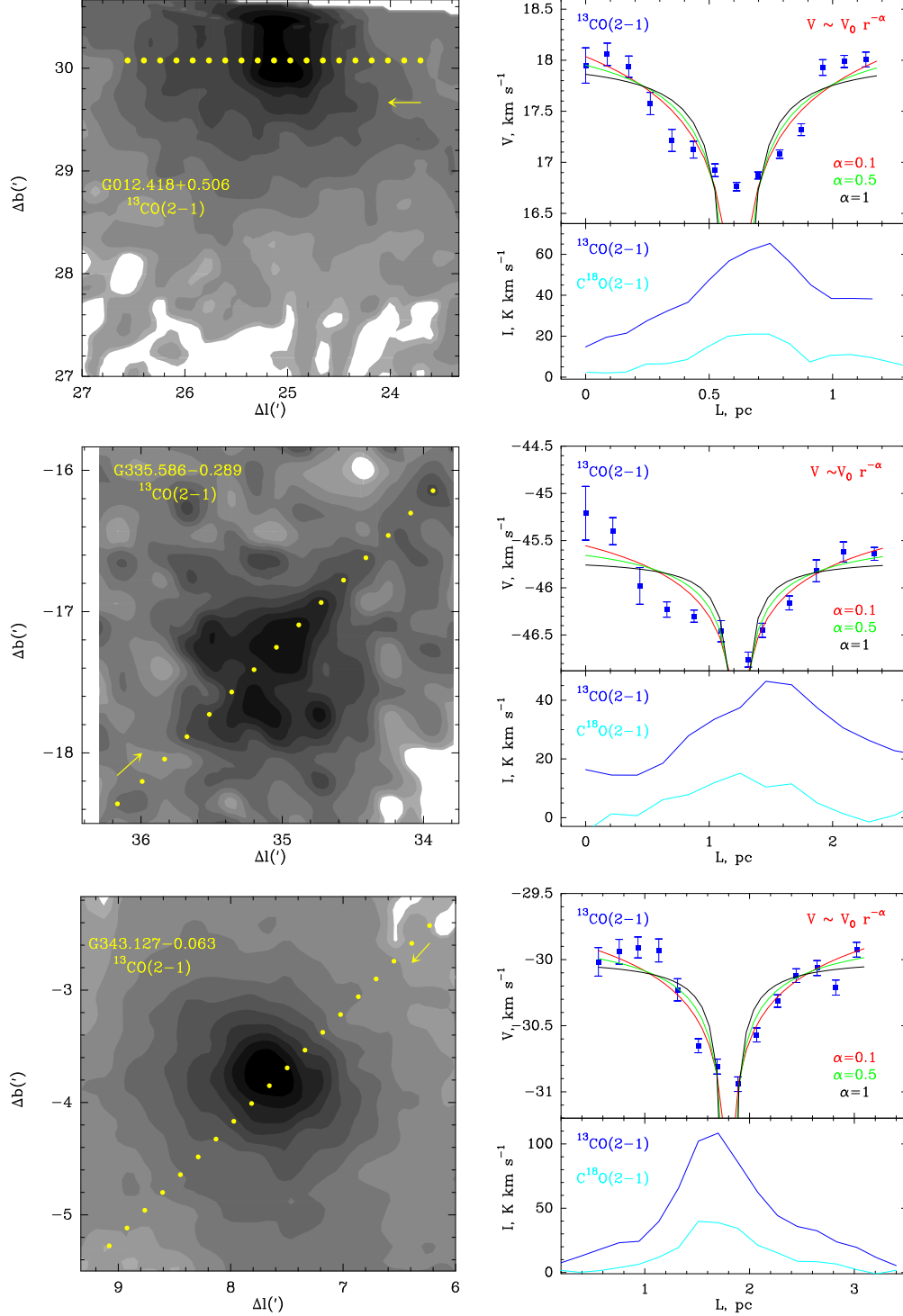


Figure 5. Maps of integrated $^{13}\text{CO}(2-1)$ intensities for three cores from the sample based on SEDIGISM data [17] (left). The axes show the offsets relative to the galactic coordinates of the region centers: $(12^\circ, 0^\circ)$, $(335^\circ, 0^\circ)$, $(343^\circ, 0^\circ)$, respectively. The maps show the positions for which the velocities of the line centers and their errors were calculated from the Gaussian approximation of the $^{13}\text{CO}(2-1)$ lines. The arrows indicate the directions along which the velocity profiles and integrated intensities of $^{13}\text{CO}(2-1)$ and $\text{C}^{18}\text{O}(2-1)$ were calculated. These profiles, converted from angular units to linear units taking into account the distances to the objects (Table 1), are shown in the graphs on the right. Smooth curves of different colors correspond to the results of fitting the model dependences of the velocity on the distance with different power exponents.